RSC Advances

PAPER

View Article Online
View Journal | View Issue

Cite this: *RSC Adv.*, 2017, **7**, 4260

Electrical anisotropy and multidimensional pressure sensor of aligned Fe_3O_4@silver nanowire/polyaniline composite films under an extremely low magnetic field

Fang Fang,[ac] Yuan-Qing Li,[b] Gui-Wen Huang,[a] Hong-Mei Xiao,[a] Qing-Ping Feng,[a] Ning Hu[b] and Shao-Yun Fu*[ab]

A low magnetic field is preferred in preparing aligned composites since a high magnetic field may be harmful to human health. In this study, fine-sized Fe_3O_4 nanoparticles with diameters of several nanometers are decorated on the surface of Ag-NWs (Fe_3O_4@Ag-NWs). Controllably aligned Fe_3O_4@Ag nanowire (Ag-NW)/polyaniline (PANI) composite films are then prepared under an extremely low magnetic field of 26–42 mT, which is much lower than those reported previously (0.1–10 T). As a result, the as-prepared Fe_3O_4@Ag-NW/PANI composite films show an excellent electrical conductivity from 5.5×10^2 to 4.1×10^3 S cm^{-1} and a controllable electrical conductivity anisotropy from 1.1 to 6.7. Furthermore, the anisotropic responsive behavior of the Fe_3O_4@Ag-NW/PANI composite film makes it an ideal candidate for the fabrication of multidimensional pressure sensors. In most studies, conventional strain sensors are fabricated because they are only capable of detecting strains in one single direction due to a strongly coupled electrical conductance change. Finally, the fabrication of a multidimensional pressure sensor based on the as-prepared Fe_3O_4@Ag-NW/PANI composite film is demonstrated for the first time and a unique anisotropic pressure sensitivity is reported.

Received 12th October 2016
Accepted 15th November 2016

DOI: 10.1039/c6ra25128e

www.rsc.org/advances

1. Introduction

Nowadays, one and two-dimensional nanomaterials, including silver nanowires (Ag-NWs),[1,2] carbon nanotubes (CNTs),[3,4] graphene,[5,6] and graphene oxide (GO),[7,8] have been extensively studied not only due to their superior electrical conductivities, but also their anisotropic nature. The anisotropic properties of these nanomaterials are strongly dependent on the structure of their assemblies. Various advanced functional materials such as transparent films,[9,10] thermal conductive films,[11,12] ion-exchange membranes[13] and liquid-crystalline films,[14] have been fabricated based on anisotropic nanostructures such as arrays, sheets and ropes. These anisotropic nanostructures were constructed *via* various methods, such as external electrical/magnetic field-assisted fabrication,[3,7] chemical-vapor-deposition-grown method,[12,15] self-assembly,[8,16] electro-synthesis,[17] mechanical shear[4] like stretching,[18] spinning[19] and extrusion,[20] thermal press[21] and annealing.[22] Among these, a magnetic field-assisted process is attractive due to its ease in controlling anisotropic nanostructures in the macro-range.[23] Anisotropic nanomaterials such as CNTs,[24,25] graphene oxides,[7,8] boron nitride platelets,[26] and Ag–Ni micro-particles[27] have been successfully aligned by applying magnetic fields.

Polymer nanocomposites that are lightweight and fabricated using simple techniques are highly attractive because their properties are tunable by controlling filler type and content. Recently, considerable attention has been paid to orientated anisotropic nanomaterial/polymer composites.[16,26,28] Yousefi *et al.* prepared an aligned reduced GO (r-GO)/epoxy composite as a high performance electromagnetic interference shielding material.[8] Wu *et al.* aligned GO in acryl monomers to yield reduced GO hybridized hydrogels that possess anisotropic electro-conductivity.[7] Wang *et al.* transferred CNT arrays onto flexible epoxy composite films with excellent thermal conductivity along the thickness direction.[12] Owing to their unique electrical, optical and thermal properties, oriented Ag-NWs demonstrate wide applications in microelectronic and[29,30] optoelectronic devices[31–33] and electromechanical systems.[34] Liu *et al.* revealed that the effective field-effect mobility of the thin-film transistors can be enhanced with the incorporation of Ag-NW arrays.[30] The anisotropy of the surface enhanced Raman scattering spectra of aligned Ag-NW films was reported by Zhou *et al.*[32] In previous reports, most of the Ag-NWs were orientated with the assistance of templates.[35–37] However, to the best of our knowledge, the alignment of Ag-NWs with a magnetic field

[a]*Technical Institute of Physics and Chemistry, Chinese Academy of Sciences, Beijing 100190, China. E-mail: syfu@mail.ipc.ac.cn; syfu@cqu.edu.cn*
[b]*College of Aerospace Engineering, Chongqing University, Chongqing 400044, China*
[c]*University of Chinese Academy of Sciences, Beijing 100049, China*

assisted process has been rarely reported, particularly under a relatively low field strength. Most alignments require enormous field strengths, of the order of 0.1–10 T,[7,29,38–40] which severely hinders their practical applications since high magnetic fields may be harmful to human health.

Polyaniline (PANI) has been well accepted as a matrix for preparing conducting polymer composites due to its ease of fabrication, low cost, *etc.* Herein, layer-structured PANI composite films with aligned Ag-NWs were prepared *via* a magnetic field-assisted casting method. To easily tailor the alignment of the Ag-NWs, Fe_3O_4 nanoparticles, used as magnetic carriers with excellent magnetic characteristics, were decorated on the surfaces of the Ag-NWs by a simple solvothermal method. The effects of magnetic field intensity, structure and filler content of the Fe_3O_4@Ag-NWs on the anisotropic behavior of the composite films were systematically evaluated. Finally, a strain sensor with significant anisotropic responsive behavior is demonstrated with the as-prepared Fe_3O_4@Ag-NW/PANI composite films as strain sensitive materials. It is well known that conventional strain sensors are only capable of detecting strains in one single direction because they usually show a strong coupled electrical conductance change in the principal strain direction and the perpendicular direction due to Poisson's ratio.[41,42] The anisotropic responsive behavior of the Fe_3O_4@Ag-NW/PANI composite films make the decoupled electrical response possible, which is ideal for the fabrication of multidimensional strain sensors with applications in tactile skin, robotic control, *etc.*[10,19,43,44]

2. Experimental

2.1 Materials

Silver nitrate ($AgNO_3$), poly(*N*-vinylpyrrolidone) (PVP, MW = *ca.* 50 000), ethylene glycol (EG), hexahydrated ferric chloride ($FeCl_3 \cdot 6H_2O$), ferrous sulfate ($FeSO_4 \cdot 7H_2O$), sodium hydroxide (NaOH), aniline, ammonium persulfate (APS), HCl, *n*-butanol, $NH_3 \cdot H_2O$, *N*-methyl-2-pyrrolidone (NMP), polydimethylsiloxane (PDMS), acetone and ethanol were all of analytical grade and purchased from Lan Yi Co. Ltd, Beijing, China. Except that aniline was further treated with vacuum distillation, all chemicals were used as received.

2.2 Preparation of Ag-NWs and Fe_3O_4@Ag-NWs

Ag-NWs were prepared *via* a solvothermal method.[1] In a typical route, 16.65 g PVP was thoroughly dissolved in a 200 ml EG solution of $FeCl_3$ (0.01 mM). Then, the well-mixed solution was dripped into a 200 ml EG solution of $AgNO_3$ (0.1 M) under continuous stirring. The obtained mixture was sealed in a 500 ml Teflon-lined stainless steel autoclave and allowed to react for 3 h at 160 °C to form Ag-NWs. The as-synthesized Ag-NWs were washed with acetone and ethanol, sequentially. Finally, the Ag-NWs were re-dispersed in EG for further use.

Fe_3O_4@Ag-NWs were synthesized *via* a similar solvothermal method described as follows: 0.07 g of $FeCl_3 \cdot 6H_2O$ and 0.036 g of $FeSO_4 \cdot 7H_2O$ were dissolved in 43 ml of EG at 50 °C. Afterward, 30 ml of EG dispersed with 0.3 g of Ag-NWs was added into the obtained solution. The mixture was stirred for 20 min at 65 °C, and then 5 ml of a EG solution dissolved with 0.1 g NaOH was added dropwise. After stirring for 20 min, the suspension was transferred into a Teflon-lined stainless steel autoclave and heated at 200 °C for 4 h. The products obtained were washed with ethanol several times. In this process, EG plays a critical role as a reductant and solvent, simultaneously. Based on the feeding ratio of the Fe^{3+}/Fe^{2+} ions, the concentration of reactant mixtures were controlled from 0.90 to 0.18 g l^{-1} for $FeCl_3$ and from 0.46 to 0.09 g l^{-1} for $FeCl_2$. When the weight ratio of Fe_3O_4 to Ag-NWs is changed from 0.02 to 0.04, 0.06, 0.08, and 0.1, the Fe_3O_4@Ag-NW is hereafter referred to as $FA_{0.02}$, $FA_{0.04}$, $FA_{0.06}$, $FA_{0.08}$ and $FA_{0.1}$, respectively.

2.3 Preparation of anisotropic Fe_3O_4@Ag-NW/PANI conductive films

PANI, a typical linear conducting polymer[45] with low cost and high anti-corrosion property,[2,46] was prepared by oxidative polymerization of aniline.[46] A specific example was given as follows: 20 ml of freshly distilled aniline monomer was dispersed in an HCl solution (2.7 mol l^{-1}, 100 ml) and APS (2.2 mol l^{-1}, 50 ml) was then slowly added dropwise under vigorous stirring. The polymerization was carried out at 0–5 °C under stirring for 24 h. The prepared emeraldine salt form of PANI was washed with deionized water several times. To convert the emeraldine salt form of PANI into the base form, the prepared PANI was dispersed in 100 ml of ammonium hydroxide (28%) and kept stirring for 24 h and then washed with deionized water and ethanol several times. A PANI solution was prepared by dissolving 0.4 g of PANI powder in 40 ml of NMP, and the insoluble residues were removed by centrifugation.

The composite films of Fe_3O_4@Ag-NW/PANI were prepared using a two-step casting method reported in our previous report.[47] It is depicted as follows: Fe_3O_4@Ag-NWs dispersed in *n*-butanol (10 mg ml^{-1}) with a calculated volume was dropped onto a glass substrate with a tunable magnetic field. After *n*-butanol was evaporated completely, 2.5 ml of a PANI solution was dropped onto the surface of the Fe_3O_4@Ag-NW layer and then NMP was removed with an infrared light. The resultant Fe_3O_4@Ag-NW/PANI composite film was peeled off of the glass substrate for further measurements.

2.4 Testing methods

The morphologies of the Fe_3O_4@Ag-NWs and Fe_3O_4@Ag-NW/PANI composite films were examined using a scanning electron microscope (SEM, Hitachi S-4300, Japan). The morphology of the Fe_3O_4@Ag-NWs was also observed with a transmission electron microscope (TEM, JEM2100, Japan). Nano Measurer Software was used to estimate the average diameter and length of the nanomaterials. Magnetic hysteresis curves of Fe_3O_4@Ag-NWs were measured using a vibrating sample magnetometer (VSM, Lakeshore7307, USA). X-ray diffraction (XRD) of the composite film was performed on an X-ray diffractometer (D8 focus) with Cu Kα radiation ($\lambda = 0.154$ nm) with 2θ values from 10° to 90°. Surface analysis of the Fe_3O_4@Ag-NWs was

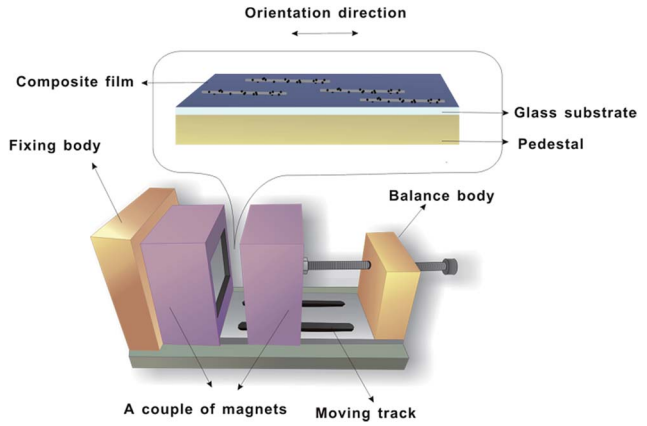

Fig. 1 Schematic of the magnetic device with tunable magnetic field intensity.

performed using X-ray photoelectron spectroscopy (XPS, ESCALAB 250Xi, Thermo Fisher) under 300 W Al Kα radiation. Fourier transform infrared (FT-IR) spectra were recorded with a Bruker Tensor 27 spectrometer using the attenuated total reflection technique. The electrical conductivities of the Fe_3O_4@Ag-NWs and composite films were measured with a Keithley Source Meter 2400 by a standard four-probe method, and average results were obtained from at least three samples. The Fe_3O_4@Ag-NWs in the form of pressed laminates (20 MPa of applied stress) with a thickness of 75 μm were used for the electrical conductivity test. Tensile tests were performed on an Instron 5882 with a loading speed of 1 mm min^{-1}. The dimensions of the specimens were 10 × 60 mm^2, and at least four specimens for each formulation were measured. As displayed in Fig. 1, the intensity of the magnetic field was controlled by adjusting the distance between the two magnets. A Teslameter (SG-3-A, Beijing Zhuo Sheng Jia Co. Ltd.) was used to measure the magnetic field strength. The composite film was sealed with 20 g of PDMS to examine its tactile sensing behavior with copper wires adhered onto the composite film as electrodes.

3. Results and discussion

3.1 Morphology and characteristics

As shown in Fig. 2, the as-synthesized Ag-NWs have a typical wire like structure. The average diameter and length of the pristine Ag-NWs are 910 nm and 31.2 μm, respectively, which is measured based on 100 nanowires. The microstructure of the Ag-NWs decorated with fine-sized Fe_3O_4 with a diameter of a few nm is presented in Fig. 3. It can be seen that the Fe_3O_4 nanoparticles were randomly distributed on the surface of the Ag-NWs as patches of aggregated clusters. In addition, the size of the Fe_3O_4 clusters on the surface of the Ag-NWs increased with an increasing amount of iron salt, indicating that the structure of the Fe_3O_4@Ag-NWs is tunable by controlling the volume of reacting agents added.

To analyze the crystal structure, the XRD pattern of the as-synthesized Fe_3O_4@Ag-NW/PANI composite film is presented in Fig. 4. The broad peak at 19.85° is attributed to the periodicities parallel to the amorphous polymer chain.[48] The diffraction peaks at 38.1°, 44.3°, 64.4°, 77.4° and 81.5° correspond to the (111), (200), (220), (311) and (222) planes, respectively, of the Ag-NWs. The reflection peaks appearing at 30.1°, 35.5°, 53.6°, 57.1°, 62.7° and 74.9° are indexed to the (220), (311), (422), (511), (440) and (533) planes of Fe_3O_4, respectively, which confirms the formation of Fe_3O_4 nanoparticles. Furthermore, the lattice spacing "*d*" for the (311) plane was calculated using the Bragg equation and is about 2.53 Å, which matches well with the standard value of 2.532 Å.[26]

XPS was performed to examine the chemical composition of the prepared Fe_3O_4@Ag-NWs (Fig. 5). In Fig. 5b, two peaks with binding energies of 710.8 and 724.3 eV, corresponding to Fe $2p_{3/2}$ and Fe $2p_{1/2}$ respectively,[49] are seen, without a satellite peak situated at 719 eV, which is a major characteristic of γ-Fe_2O_3. In the O core level spectrum (Fig. 5c), the main peak at 530.2 eV is attributed to the oxygen atoms in Fe_3O_4. The binding energy values at 368.2 eV and 374.2 eV for Ag $3d_{3/2}$ and Ag $3d_{5/2}$,

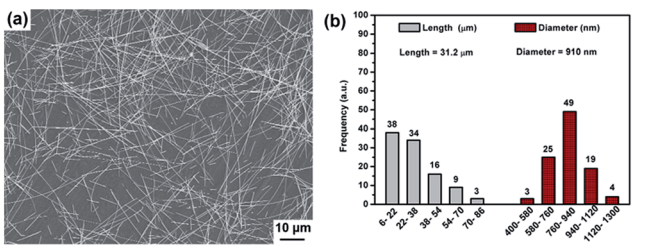

Fig. 2 (a) SEM image of Ag-NWs and (b) histogram for the length and diameter of Ag-NWs.

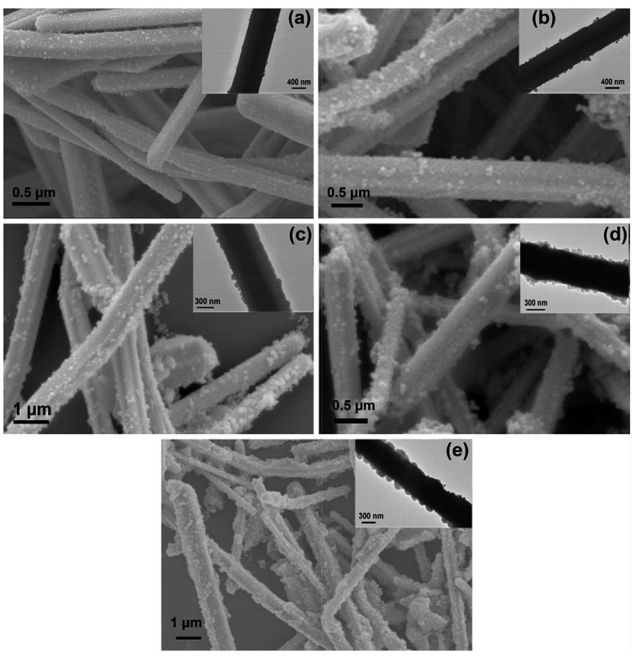

Fig. 3 SEM images of Fe_3O_4@Ag-NWs for (a) $FA_{0.02}$, (b) $FA_{0.04}$, (c) $FA_{0.06}$, (d) $FA_{0.08}$ and (e) $FA_{0.1}$; insets are the corresponding TEM images.

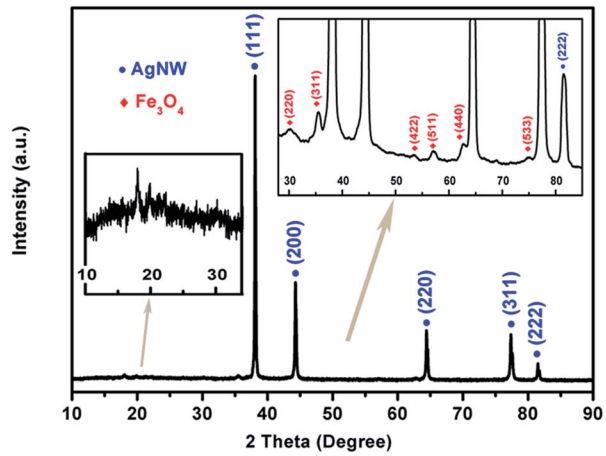

Fig. 4 XRD patterns of $FA_{0.1}$/PANI composite film. The insets are parts of enlarged XRD patterns.

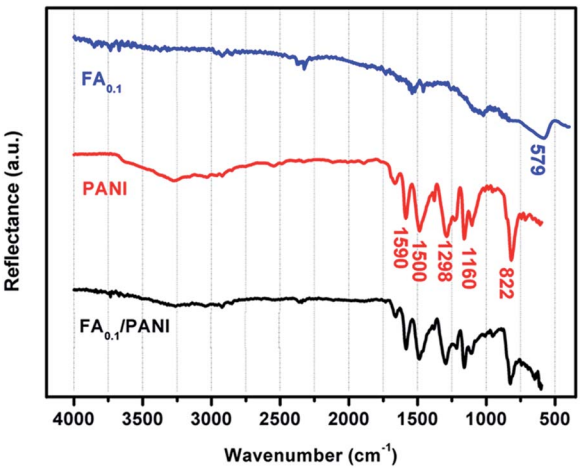

Fig. 6 FT-IR spectra of $FA_{0.1}$, pure PANI film and $FA_{0.1}$/PANI composite film.

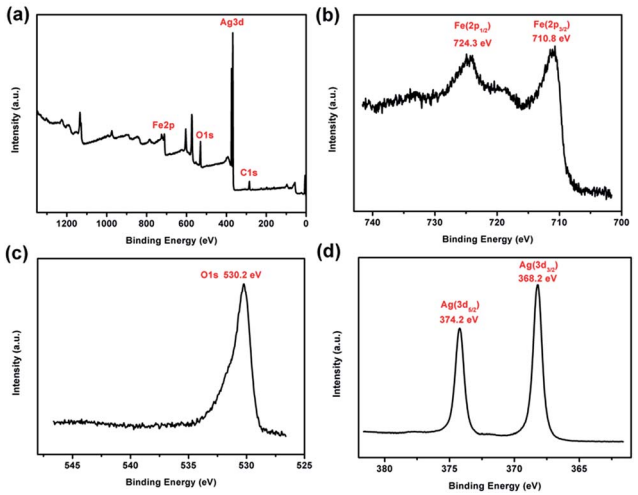

Fig. 5 (a) XPS survey spectrum, (b) Fe 2p, (c) O 1s and (d) Ag 3d high resolution spectra of the $FA_{0.1}$.

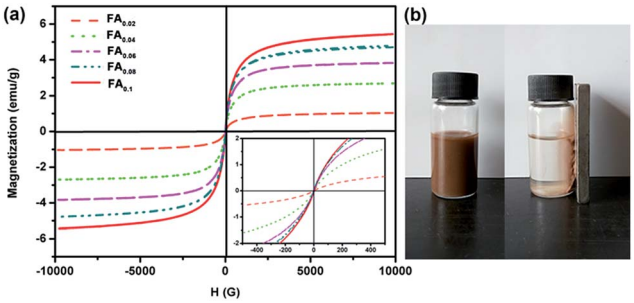

Fig. 7 (a) Magnetic hysteresis loops for Fe_3O_4@Ag-NWs with different Fe_3O_4/Ag ratios. The inset shows a close view of the hysteresis loops. (b) $FA_{0.02}$ dispersed in ethanol (left) and their magnetic separation (right).

respectively, are observed in Fig. 5d.[50] These results validate the successful formation of Fe_3O_4@Ag-NWs.

FT-IR spectra of Fe_3O_4@Ag-NWs, pure PANI films and Fe_3O_4@Ag-NW/PANI composite films are shown in Fig. 6. The peak at ~579 cm^{-1} in Fe_3O_4@Ag-NWs is attributed to the Fe–O bond vibration of Fe_3O_4. The spectrum of PANI shows the presence of quinoid and benzenoid ring stretching modes at 1590 cm^{-1} and 1500 cm^{-1}, respectively, indicating the emeraldine base form of PANI. The C–H plane-bending vibrations (1160 cm^{-1}) and C–H out-of-plane bending vibrations (822 cm^{-1}) of the PANI structure are also observed.[51] For the Fe_3O_4@Ag-NW/PANI composite film, the PANI characteristic peaks are well preserved, but the Fe–O vibration peak is invisible since the intensity of the PANI characteristic peaks is too strong.

The magnetic properties of the Fe_3O_4 decorated Ag-NWs were investigated using a vibrating sample magnetometer at room temperature, as shown in Fig. 7a. The saturation magnetization (M_s) values of the as-synthesized Fe_3O_4@Ag-NWs depend on the content of the decorated magnetic particles. The M_s values for $FA_{0.02}$, $FA_{0.04}$, $FA_{0.06}$, $FA_{0.08}$ and $FA_{0.1}$ are 1.04, 2.70, 3.82, 4.70 and 5.44 emu g^{-1}, respectively. Fig. 7b shows that $FA_{0.02}$ dispersed in ethanol can be magnetically separated from ethanol.

3.2 Electrical conductivity anisotropy of the Fe_3O_4@Ag-NW/PANI composite film

The Fe_3O_4@Ag-NWs in PANI composite films were aligned by the magnetic field, which resulted in the anisotropy of the Fe_3O_4@Ag-NW/PANI composite films. The electrical anisotropy is defined as the ratio of $\sigma_{\parallel}$ to $\sigma_{\perp}$, where $\sigma_{\parallel}$ and $\sigma_{\perp}$ are the electrical conductivities of the composite film in the direction "parallel to the alignment direction of the Fe_3O_4@Ag-NWs" (abbreviated as $NW_{\parallel}$) and "perpendicular to the alignment direction of the Fe_3O_4@Ag-NWs" (abbreviated as $NW_{\perp}$), respectively. The formation of aligned Ag-NW conductive paths promotes electron transfer along the direction of $NW_{\parallel}$ with more straight paths. As for the direction of $NW_{\perp}$, although the transverse Ag-NW to Ag-NW contact is still possible, there are

more discontinuous and separated conductive paths for electrons to travel.

The electrical conductivities of the $FA_{0.1}$/PANI composite films prepared under different magnetic fields are shown in Fig. 8. The anisotropy of the composite film significantly increases with an increase in filler content from 5 to 15 wt%, and then a slight drop in the anisotropy is seen on further increasing the filler content to 45 wt%, which relates with the conductive paths formed in the directions of $NW_{\parallel}$ and $NW_{\perp}$. With an increase in the content of $FA_{0.1}$ from 0 to 15 wt%, the composite films show a better connected conductive path in the direction of $NW_{\parallel}$ than that in the direction of $NW_{\perp}$. However, when the filler content further increases from 15 to 45 wt%, the conductive paths simultaneously grow in both directions, such that the anisotropy of the film is degenerated. In addition, the anisotropy of the as-composite films monotonically rises with an increase in the magnetic field intensity applied at the process of film preparation, and a maximum anisotropy of 6.7 is achieved for the composite film with 15 wt% $FA_{0.1}$ at a magnetic field strength of 42 mT (Fig. 8b). Nonetheless, on further increasing the applied magnetic field intensity to 46 mT, the as-prepared composite film tends to be brittle and easy to split along the direction of $NW_{\parallel}$, owing to the stress concentration of the magnetic fillers with a large amount. Hence the magnetic field intensity of 42 mT is chosen to fabricate the optimum composite films, which is much lower than that reported to be required in other studies.[7,24–26,40]

The influence of Fe_3O_4 to the Ag-NWs mass ratio ($R_{Fe/Ag}$) on the anisotropy and conductivity of the composite film was studied. The decoration of Fe_3O_4 on the surface of Ag-NWs results in a decrease of its electrical conductivity. As shown in Fig. 9a, $\sigma_{\parallel}$ of the composite film declines from 4.1×10^3 to 5.5×10^2 S cm^{-1} with the increase of $R_{Fe/Ag}$ from 0.02 to 0.1. At the same time, the anisotropy of the composite films rises with an increase in $R_{Fe/Ag}$. As revealed in Fig. 9b–f, the arranging order of the Fe_3O_4@Ag-NWs in the composite films shows an ascending trend, corresponding to the increase in the saturation magnetization values of the occupied composite filler (from $FA_{0.02}$ to $FA_{0.1}$). In addition, the intersection point of $\sigma_{\parallel}$ with anisotropy in Fig. 9a, with an $R_{Fe/Ag}$ value of 0.034, indicates the best tradeoff between the electrical conductivity and anisotropy of the corresponding composite film. Thus, $FA_{0.034}$ and $FA_{0.034}$/PANI composite films were prepared for the following study.

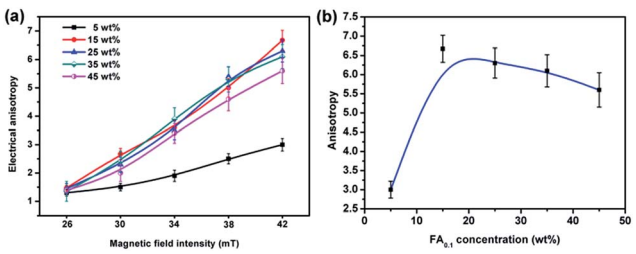

Fig. 8 (a) Anisotropy of $FA_{0.1}$/PANI composite film with various filler contents as function of magnetic field intensity. (b) Film anisotropy as function of $FA_{0.1}$ weight content in a magnetic field intensity of 42 mT.

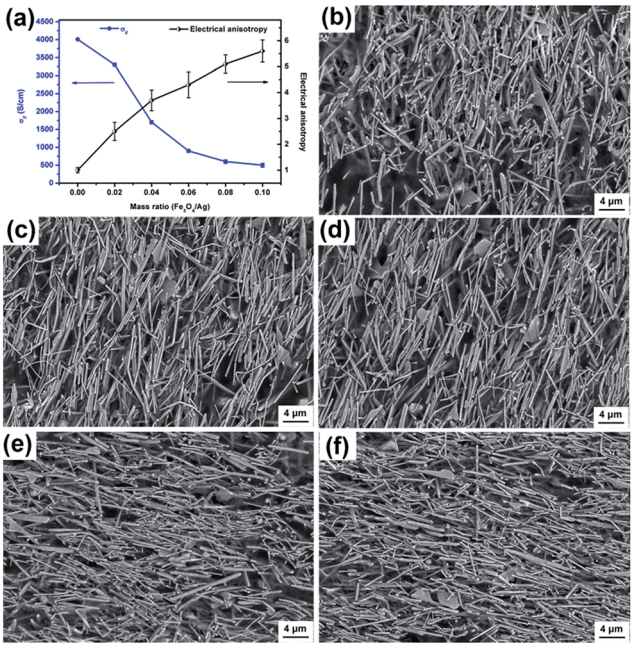

Fig. 9 (a) Anisotropy and $\sigma_{\parallel}$ of the PANI composite films with different Fe_3O_4@Ag-NWs as fillers, SEM images of the bottom surface of the PANI composite films with (b) $FA_{0.02}$, (c) $FA_{0.04}$, (d) $FA_{0.06}$, (e) $FA_{0.08}$ and (f) $FA_{0.1}$ as fillers, respectively. All of the composites films were prepared in a magnetic field intensity of 42 mT and the filler content is fixed at 45 wt%.

Anisotropic electrical conductivities have been observed in aligned films, meshes, and nanopapers fabricated by different methods. The comparison of electrical anisotropy in the present study with literature[4,8,9,18,19,24,25,39,52–58] is presented in Table 1. It is clear that the electrical anisotropy and electrical conductivity have an inverse relationship. All of composites that reported a high electrical anisotropy show a low conductivity in aligned direction. Although the electrical anisotropy of Fe_3O_4@Ag-NW/PANI composite films, reported herein, is not the highest, its electrical conductivity is the highest for the composites with the same level of anisotropy. Importantly, a trade-off between the high anisotropy and high electrical conductivity is achieved in this study.

In order to determine the percolation threshold, the electrical conductivity of the Fe_3O_4@Ag-NW/PANI composite films is fitted to a power law. According to the percolation theory, the following equation can be presented:[24]

$$\sigma \propto (v - v_c)^t \quad (1)$$

where σ is the conductivity of the composite, v is the volume fraction of the filler, v_c is the percolation threshold and t is the critical exponent. The volume of $FA_{0.034}$ is assumed to be identical with that of Ag-NWs since the value of $R_{Fe/Ag}$ is only 0.034, whereas the volume of PANI is estimated from the product thickness and area for a neat PANI film. The plots of $\log(\sigma_{\parallel})$ and $\log(\sigma_{\perp})$ *versus* $\log(v - v_c)$ are presented in Fig. 10. With linear fitting, the percolation threshold calculated along $NW_{\parallel}$ and $NW_{\perp}$ is 2 vol% (corresponding to 9.3 wt%) and 3 vol%

Table 1 Comparison of the electrical conductivity and anisotropy of the aligned composites between the references and the present study

Composites	Method	Electrical anisotropy	Conductivity in aligned direction	Filler content	Ref.
CNT/polystyrene	CVD + *in situ* polymerization	20	0.8 S cm^{-1}	20 wt%	52
CNT/poly(*p*-phenylene ethynylene)s	Self-assembly	4.1	9.2×10^{-3} S cm^{-1}	—	53
CNT/polysulfone	Electric field assisted	10^5	10^{-4} S cm^{-1}	0.2 wt%	54
PANI/montmorillonite	*In situ* polymerization + pressure	1016	8.4×10^{-2} S cm^{-1}	—	55
CNT/polyacrylonitrile	Magnetic field assisted electrospinning	15.4	3.2×10^{9} Ω □$^{-1}$	2 wt%	39
CNT/poly(methyl methacrylate) (PMMA)	Mechanical stretching	10^4	10^{-4} S cm^{-1}	1 wt%	56
CNT/PMMA	Electric field assisted thermal annealing	10^6	1.13×10^{-4} S cm^{-1}	1 wt%	57
CNT/natural rubber-nitrile rubber	Milling	10^3	3.16×10^{-6} S cm^{-1}	4 wt%	58
γ-Fe_2O_3-CNT/polythylene oxide	Magnetic field induced	10	4×10^{-6} S cm^{-1}	3 wt%	25
γ-Fe_2O_3-CNT/epoxy	Magnetic field induced	4.1	4.1×10^{-9} S cm^{-1}	1 wt%	24
Graphene nanoribbon & CNT/polyimide	Electrospinning	1.15×10^6	8.3×10^{-4} S cm^{-1}	9 wt%	19
Graphite/polyacetylene	Mechanical stretching + thermal treatment	1.1–1.3	1501 S cm^{-1}	61–74 wt%	18
r-GO/epoxy	Self-alignment	5×10^6	10^{-2} S cm^{-1}	3 wt%	8
CNT buckypaper	Shearing	~2	600 S cm^{-1}	—	4
Ag–Ni-NWs	Magnetic field induced	10^5	220 Ω □$^{-1}$	—	9
Fe_3O_4@Ag-NW/PANI	Magnetic field induced	6.7	187 S cm^{-1}	15 wt%	Present study

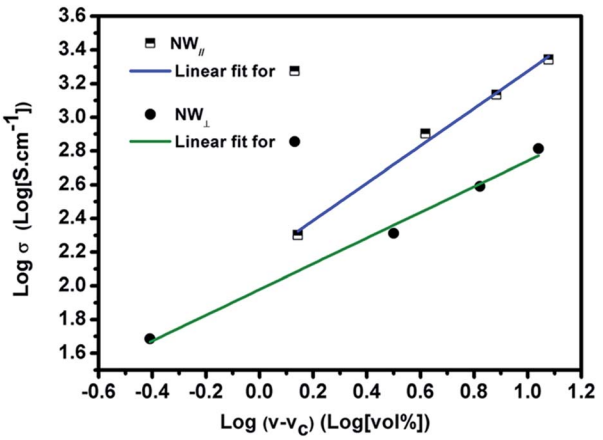

Fig. 10 Percolation equation fit to the experimental conductivity data obtained in the direction of $NW_{\parallel}$ and $NW_{\perp}$, with regression coefficients of 0.99.

(corresponding to 13.5 wt%), respectively. Thus, the Fe_3O_4@Ag-NW/PANI composite film with a filler content of 13 wt% possesses the optimal properties – the trade-off between high electrical conductivity and reasonable anisotropy.

3.3 Mechanical properties of the Fe_3O_4@Ag-NW/PANI composite film

Fig. 11 shows the typical tensile strain–stress curves of the composite films stretched along the direction of $NW_{\parallel}$ and $NW_{\perp}$, respectively. Along the direction of $NW_{\parallel}$, the film has a tensile strength and an elongation at break of 69 MPa and 2.64%, respectively. In comparison, the tensile strength and elongation at break in the direction of $NW_{\perp}$ is 60 MPa and 2.21%, respectively, which is relatively smaller than that in the direction of $NW_{\parallel}$. As expected, the composite films with aligned Fe_3O_4@Ag-NWs show anisotropic mechanical properties. Similar results were also found in the aligned CNT/PMMA system.[56,57,59] It is believed that the embedding of CNTs is supposed to introduce defects into the polymer matrix, and the defects tend to form cracks along the CNT direction, resulting in the deterioration of the mechanical property perpendicular to the CNT aligning direction.[56,59] It seems that this explanation is also plausible in this study. As shown in Fig. 12, wire-like folds appear in parallel on the top surface of the PANI composite film, which is believed to be caused by the alignment of the Ag-NWs. Both the orientated folds in the matrix and aligned Ag-NWs together are supposed to account for the anisotropic mechanical behaviour of the composite films.

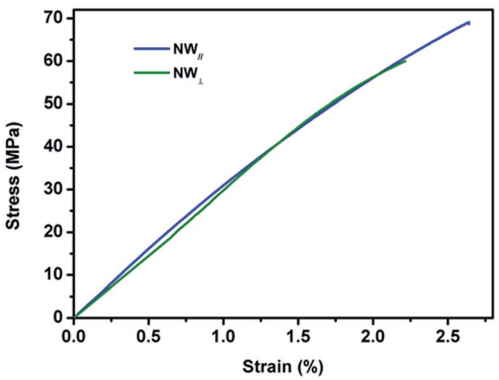

Fig. 11 Tensile stress–strain curves of the 13 wt% composite film stretched along the direction of $NW_{\parallel}$ and $NW_{\perp}$, respectively.

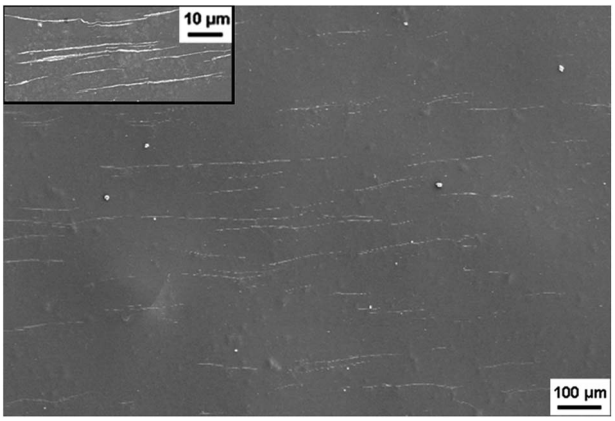

Fig. 12 SEM image of the top surface of Fe_3O_4@Ag-NW/PANI composite film, the inset is a high magnification SEM image.

3.4 Fe_3O_4@Ag-NW/PANI composite film as tactile sensor

To demonstrate the potential application of the Fe_3O_4@Ag-NW/PANI composite films, a strain sensor based on the PDMS sealed composite film was fabricated, which is mechanically robust with tactile sensibility. Fig. 13 presents the PDMS-sealed-composite film sensor for the cyclic pressing-releasing test, which shows three copper wires coming out of the sensor for resistance measurements in different directions: 1–3 for parallel direction, 2–3 for perpendicular direction.

The electrical resistances of the sensor in the direction of $NW_{\parallel}$ and $NW_{\perp}$ under repeated pressuring-releasing cycles were measured. Relative changes of the resistance (RCR, $\Delta R/R_0$) of the sensor under cyclic loading-unloading with different maximum pressures are presented in Fig. 14. In both directions, the sensor shows good responses to the applied cyclic loading.

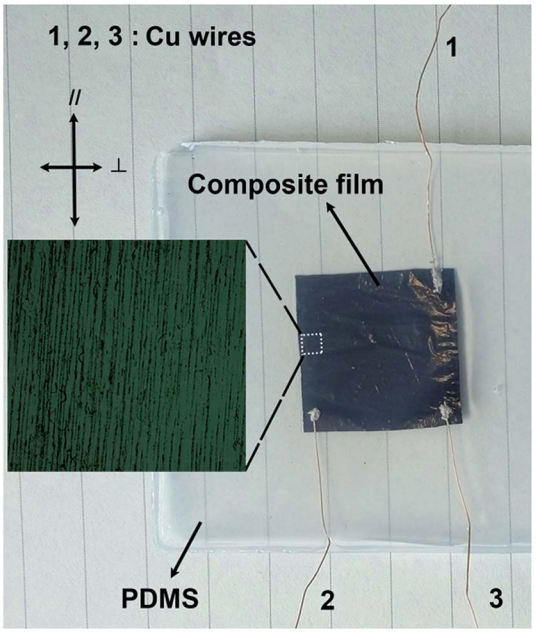

Fig. 13 PDMS-sealed composite film for tactile sensing. The inset shows the magnified aligned Ag-NWs under the optical microscope.

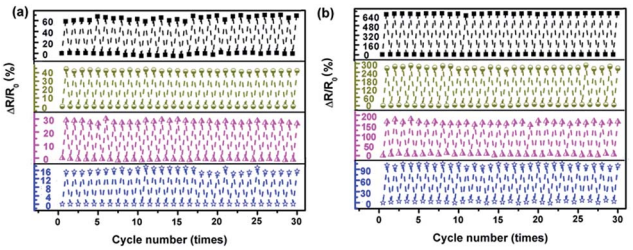

Fig. 14 The RCR response of the sensor prepared along the direction of (a) $NW_{\parallel}$ and (b) $NW_{\perp}$ within 30 loading-unloading cycles under a maximum pressure of 30 kPa (hollow pentagram), 50 kPa (semi-hollow triangle), 70 kPa (semi-hollow circle) and 90 kPa (solid square).

The RCR responses of the sensor exhibit excellent stability within the tested cycles, without any significant resistance drifting. In addition, with an increase in the maximum pressure from 30 kPa to 90 kPa, the RCR peak values of the sensor in the direction of $NW_{\parallel}$ and $NW_{\perp}$ increase from 16% to 65% and 100% to 680%, respectively. The RCR responses of the sensor are consistent and reversible within the pressure range studied, demonstrating that the composite film can work properly up to a pressure of 90 kPa.

Importantly, the RCR of the sensor in the $NW_{\perp}$ direction is 6 to 10 times higher than that in the direction of $NW_{\parallel}$ due to the anisotropy of the composite film. Because the conventional strain sensor has a strong coupled electrical resistance change in the principal strain direction and in the perpendicular direction, they are only capable of detecting strain in a single direction. This hinders their application to detect more complex multiaxial, multidimensional strain conditions.[41,42] The decoupled electrical resistance change to the major axis of the principal strain and perpendicular direction can be independently detected by assembling two Fe_3O_4@Ag-NW/PANI films intersecting each other.[41] The anisotropic responsive behavior of the Fe_3O_4@Ag-NW/PANI composite films makes it ideal for the fabrication of a multidimensional strain sensor for applications in tactile skin, robotic control, *etc.*

4. Conclusions

Layer structured PANI composite films with aligned Ag-NWs have been fabricated under an extremely low magnetic field of 26–42 mT. To control the alignment, Fe_3O_4 nanoparticles as magnetic responders are decorated on the surfaces of the Ag-NWs. The effects of magnetic-field intensity, Fe_3O_4@Ag-NW filler content and Fe_3O_4/Ag-NW ratio on the anisotropy of the composite films are clarified. Between the $NW_{\parallel}$ and $NW_{\perp}$ directions, the difference in the electrical conductivity of the composite films is in the range of 15–91%. For the composite film with 13 wt% Fe_3O_4@Ag-NWs (the Fe_3O_4/Ag-NWs ratio is 0.034), there is an 87% difference in tensile strength and an 84% difference in elongation at break. Finally, an anisotropic multidimensional pressure sensor is demonstrated based on the Fe_3O_4@Ag-NW/PANI composite film, which exhibits a unique anisotropic pressure responsive behavior. The relative

resistance change of the as-prepared sensor in the direction of $NW_{\perp}$ is 6 to 10 times higher than that in the direction of $NW_{\parallel}$.

Acknowledgements

This study is financially supported by the National Natural Science Foundation of China (No. 11372312 and 11572321).

Notes and references

1 Y. H. Ji, Y. Liu, G. W. Huang, X. J. Shen, H. M. Xiao and S. Y. Fu, *ACS Appl. Mater. Interfaces*, 2015, **7**, 8041–8052.
2 G. W. Huang, H. M. Xiao and S. Y. Fu, *ACS Nano*, 2015, **9**, 3234–3242.
3 R. J. Castellano, C. Akin, G. Giraldo, S. Kim, F. Fornasiero and J. W. Shan, *J. Appl. Phys.*, 2015, **117**, 214306.
4 D. Vennerberg and M. R. Kessler, *Carbon*, 2014, **80**, 433–439.
5 Z. Xu, Y. Zhang, P. G. Li and C. Gao, *ACS Nano*, 2012, **6**, 7103–7113.
6 L. Ding, L. P. Liu, P. G. Li, F. Z. Lv, W. S. Tong and Y. H. Zhang, *J. Appl. Polym. Sci.*, 2016, **133**, 43041.
7 L. L. Wu, M. Ohtani, M. Takata, A. Saeki, S. Seki, Y. Ishida and T. Aida, *ACS Nano*, 2014, **8**, 4640–4649.
8 N. Yousefi, X. Y. Sun, X. Y. Lin, X. Shen, J. J. Jia, B. Zhang, B. Z. Tang, M. S. Chan and J.-K. Kim, *Adv. Mater.*, 2014, **26**, 5480–5487.
9 B.-T. Liu, S. X. Huang, M. F. Lai and Z. H. Wei, *RSC Adv.*, 2015, **5**, 1684–1689.
10 K. Liu, Y. H. Sun, P. Liu, X. Y. Lin, S. S. Fan and K. L. Jiang, *Adv. Funct. Mater.*, 2011, **21**, 2721–2728.
11 H. Jung, S. Yu, N.-S. Bae, S. M. Cho, R. H. Kim, S. H. Cho, I. Hwang, B. Jeong, J. S. Ryu, J. Hwang, S. M. Hong, C. M. Koo and C. Park, *ACS Appl. Mater. Interfaces*, 2015, **7**, 15256–15262.
12 M. Wang, H. Y. Chen, W. Lin, Z. Li, Q. Li, M. H. Chen, F. C. Meng, Y. J. Xing, Y. G. Yao, C. P. Wong and Q. W. Li, *ACS Appl. Mater. Interfaces*, 2014, **6**, 539–544.
13 N. V. Loza, S. A. Loza, N. A. Kononenko and A. V. Magalyanov, *Pet. Chem.*, 2015, **55**, 724–729.
14 R. Schaller, T. Peijs and T. A. Tervoort, *Composites, Part A*, 2016, **81**, 296–304.
15 X. Liu, X. Y. Sun, Z. Y. Wang, X. Shen, Y. Wu and J.-K. Kim, *ACS Appl. Mater. Interfaces*, 2015, **7**, 21455–21464.
16 R. O. Mäkiniemi, P. Das, D. Hönders, K. Grygiel, D. Cordella, C. Detrembleur, J. Y. Yuan and A. Walther, *ACS Appl. Mater. Interfaces*, 2015, **7**, 15681–15685.
17 B. Endrodi, G. F. Samu, D. Fejes, Z. Nemeth, E. Horvath, A. Pisoni, P. K. Matus, K. Hernadi, C. Visy, L. Forro and C. Janaky, *J. Polym. Sci., Part B: Polym. Phys.*, 2015, **53**, 1507–1518.
18 S. Matsushita and K. Akagi, *J. Am. Chem. Soc.*, 2015, **137**, 9077–9087.
19 M. K. Liu, Y. F. Du, Y.-E. Miao, Q. W. Ding, S. X. He, W. W. Tjiu, J. S. Pan and T. X. Liu, *Nanoscale*, 2015, **7**, 1037–1046.
20 M. Antunes, M. Mudarra and J. I. Velasco, *Carbon*, 2011, **49**, 708–717.
21 P.-M. Geffroy, T. Chartier and J.-F. Silvain, *J. Eur. Ceram. Soc.*, 2007, **27**, 291–299.
22 Z. Qiang, Y. Z. Zhang, Y. Wang, S. M. Bhaway, K. A. Cavicchi and B. D. Vogt, *Carbon*, 2015, **82**, 51–59.
23 A. Malvandi, *J. Magn. Magn. Mater.*, 2016, **406**, 95–102.
24 I. T. Kim, A. Tannenbaum and R. Tannenbaum, *Carbon*, 2011, **49**, 54–61.
25 I. T. Kim, J. H. Lee, M. L. Shofner, K. Jacob and R. Tannenbaum, *Polymer*, 2012, **53**, 2402–2411.
26 H. S. Lim, J. W. Oh, S. Y. Kim, M.-J. Yoo, S.-D. Park and W. S. Lee, *Chem. Mater.*, 2013, **25**, 3315–3319.
27 T. Lu, J. Wissman, Ruthika and C. Majidi, *ACS Appl. Mater. Interfaces*, 2015, **7**, 26923–26929.
28 S. Gong, Z. H. Zhu and S. A. Meguid, *Polymer*, 2015, **56**, 498–506.
29 O. Trotsenko, A. Tokarev, A. Gruzd, T. Enright and S. Minko, *Nanoscale*, 2015, **7**, 7155–7161.
30 H. C. Liu, Y. C. Lai, C.-C. Lai, B. S. Wu, H.-W. Zan, P. Yu, Y.-L. Chueh and C.-C. Tsai, *ACS Appl. Mater. Interfaces*, 2015, **7**, 232–240.
31 G. Chu, X. S. Wang, T. R. Chen, J. X. Gao, F. Y. Gai, Y. Wang and Y. Xu, *ACS Appl. Mater. Interfaces*, 2015, **7**, 11863–11870.
32 W. P. Zhou, A. M. Hu, S. Bai, Y. Ma and D. Bridges, *RSC Adv.*, 2015, **5**, 39103–39109.
33 B. Park, I.-G. Bae and Y. H. Huh, *Sci. Rep.*, 2016, **6**, 19485.
34 F. Xu and Y. Zhu, *Adv. Mater.*, 2012, **24**, 5117–5122.
35 X. C. Yang, X. Zou, Y. Liu, X. N. Li and J. W. Hou, *Mater. Lett.*, 2010, **64**, 1451–1454.
36 Z. Ye, F. Guang Tao, C. Ping, W. Bing, W. Biao and Z. Li De, *Nanotechnology*, 2008, **19**, 285711.
37 G. Riveros, S. Green, A. Cortes, H. Gómez, R. E. Marotti and E. A. Dalchiele, *Nanotechnology*, 2006, **17**, 561.
38 J. A. Marins, A. Mija, J.-M. Pin, F. Giulieri, B. G. Soares, N. Sbirrazzuoli, P. Lançon and G. Bossis, *Compos. Sci. Technol.*, 2015, **112**, 34–41.
39 L.-Y. Mei, P. Song and Y.-Q. Liu, *J. Appl. Polym. Sci.*, 2015, **132**, 41995.
40 Z. H. I. Sun, X. Guo, M. Guo, J. Vleugels, O. Van der Biest and B. Blanpain, *J. Alloys Compd.*, 2013, **551**, 568–577.
41 K. K. Kim, S. Hong, H. M. Cho, J. Lee, Y. D. Suh, J. Ham and S. H. Ko, *Nano Lett.*, 2015, **15**, 5240–5247.
42 S.-H. Bae, Y. Lee, B. K. Sharma, H.-J. Lee, J.-H. Kim and J.-H. Ahn, *Carbon*, 2013, **51**, 236–242.
43 O. Gennari, S. Grilli, S. Coppola, V. Pagliarulo, V. Vespini, G. Coppola, S. Bhowmick, M. A. Gioffré, G. Gentile, V. Ambrogi, P. Cerruti, C. Carfagna and P. Ferraro, *Langmuir*, 2013, **29**, 15503–15510.
44 H. Dana and C. Nikolaus, *Bioinspiration Biomimetics*, 2015, **10**, 055002.
45 Y. Yan, J. Fang, Y. J. Zhang, H. L. Fan and Z. X. Wei, *Macromol. Rapid Commun.*, 2011, **32**, 1640–1644.
46 H. M. Xiao, W. D. Zhang, C. Lv, S. Y. Fu, M. X. Wan and Y. W. Mai, *Macromol. Chem. Phys.*, 2010, **211**, 1109–1116.
47 F. Fang, Y. Q. Li, H. M. Xiao, N. Hu and S. Y. Fu, *J. Mater. Chem. C*, 2016, **4**, 4193–4203.
48 M. Faisal and S. Khasim, *J. Mater. Sci.: Mater. Electron.*, 2013, **24**, 2202–2210.

49 N. Li, G. W. Huang, X. J. Shen, H. M. Xiao and S. Y. Fu, *J. Mater. Chem. C*, 2013, **1**, 4879–4884.
50 N. Li, G. W. Huang, H. M. Xiao and S. Y. Fu, *Composites, Part A*, 2015, **77**, 87–95.
51 A. Khan, A. Aslam Parwaz Khan, A. M. Asiri, M. Abdul Rub and N. Azum, *Polym. Compos.*, 2014, **35**, 1436–1443.
52 K. K. K. Koziol, S. Boncel, M. S. P. Shaffer and A. H. Windle, *Compos. Sci. Technol.*, 2011, **71**, 1606–1611.
53 N. Adachi, T. Fukawa, Y. Tatewaki, H. Shirai and M. Kimura, *Macromol. Rapid Commun.*, 2008, **29**, 1877–1881.
54 A. I. Oliva-Avilés, F. Avilés, V. Sosa, A. I. Oliva and F. Gamboa, *Nanotechnology*, 2012, **23**, 465710.
55 J. Tokarský, L. Kulhánková, V. Stýskala, K. Mamulová Kutláková, L. Neuwirthová, V. Matějka and P. Čapková, *Appl. Clay Sci.*, 2013, **80–81**, 126–132.
56 J. F. Dai, Q. Wang, W. X. Li, Z. Q. Wei and G. J. Xu, *Mater. Lett.*, 2007, **61**, 27–29.
57 L. Valentini, S. B. Bon and J. M. Kenny, *Macromol. Mater. Eng.*, 2008, **293**, 867–871.
58 P. Kueseng, P. Sae-oui, C. Sirisinha, K. I. Jacob and N. Rattanasom, *Polym. Test.*, 2013, **32**, 1229–1236.
59 W. X. Li, Q. Wang and J. F. Dai, *Bull. Mater. Sci.*, 2006, **29**, 313–316.

